Epitaxial growth, structural characterization, and exchange bias of noncollinear antiferromagnetic Mn_3Ir thin films

James M. Taylor,[1,*] Edouard Lesne,[1] Anastasios Markou,[2] Fasil Kidane Dejene,[1] Benedikt Ernst,[2] Adel Kalache,[2] Kumari Gaurav Rana,[1] Neeraj Kumar,[1] Peter Werner,[1] Claudia Felser,[2] and Stuart S. P. Parkin[1,†]

[1]*Max Planck Institute of Microstructure Physics, Weinberg 2, 06120 Halle (Saale), Germany*

[2]*Max Planck Institute for Chemical Physics of Solids, Nöthnitzer Str. 40, 01187 Dresden, Germany*

(Received 13 March 2019; published 30 July 2019)

Antiferromagnetic materials are of great interest for spintronics. Here we present a comprehensive study of the growth, structural characterization, and resulting magnetic properties of thin films of the noncollinear antiferromagnet Mn_3Ir. Using epitaxial engineering on MgO (001) and Al_2O_3 (0001) single-crystal substrates, we control the growth of cubic γ-Mn_3Ir in both (001) and (111) crystal orientations, and discuss the optimization of growth conditions to achieve high-quality crystal structures with low surface roughness. Exchange bias is studied in bilayers, with exchange bias fields as large as -29 mT (equivalent to a unidirectional anisotropy constant of $0.115\,\mathrm{erg\,cm^{-2}}$ or $11.5\,\mathrm{nJ\,cm^{-2}}$) measured in Mn_3Ir (111)/Permalloy heterostructures at room temperature. In addition, a distinct dependence of blocking temperature on in-plane crystallographic direction in Mn_3Ir (001)/Permalloy bilayers is observed. These findings are discussed in the context of antiferromagnetic domain structures, and will inform progress towards chiral antiferromagnetic spintronic devices.

DOI: 10.1103/PhysRevMaterials.3.074409

I. INTRODUCTION

Artificial (or synthetic) antiferromagnetic structures (SAFs) [1,2] have played a key role in spintronics since the invention of the spin-valve sensor for detecting tiny magnetic fields in magnetic recording read heads [3] and in magnetic tunnel junction (MTJ) memory bits for magnetic random access memory (MRAM) applications [4]. More recently, highly efficient current-driven motion of domain walls in SAFs was discovered [5], which makes possible racetrack memory devices [6] by utilizing the chirality of the magnetic structure [7]. SAFs and related multilayers are used to eliminate long-range magnetostatic fields that otherwise make nanoscopic spin valves and MTJs inoperable. Furthermore, the resonance frequencies of antiferromagnet (AF) materials can be much higher than of ferromagnet (FM) materials [8], making such materials of interest for ultrafast spin dynamics.

Motivated by these improvements in performance, the field of antiferromagnetic spintronics has rapidly grown [9], investigating a range of different materials. More recent experimental observations include spin-orbit torque switching and electrical readout of the AF state in CuMnAs [10], Mn_2Au [11], and MnTe [12], as well as spin currents and spin Hall magnetoresistance effects in MnPt [13,14]. Understanding of AF domain structure is important for the efficient control of the above effects in these metallic materials, all of which exhibit collinear AF order.

Materials with a noncollinear spin texture, such as Mn_3X (X = Ir, Pt, Sn, Ge), are promising candidates for *topological* AF spintronic applications [15]. This follows the prediction of an intrinsic anomalous Hall effect (AHE) in the $L1_2$ ordered phase of cubic Mn_3Ir [16]. In addition, a facet-dependent spin Hall effect (SHE) has been measured in epitaxial thin films of Mn_3Ir [17], whose origin derives from a Berry curvature-driven effective field generated by a combination of spin-orbit coupling and symmetry breaking arising from the *chiral* AF structure [17,18].

For the related compounds Mn_3Sn and Mn_3Ge, subsequent to theoretical predictions [19], large AHE has been experimentally demonstrated in highly ordered bulk samples [20,21]. This has been enabled by the ability to align a small geometrically frustrated uncompensated in-plane magnetization via an external magnetic field, in turn coherently orienting the triangular spin configuration throughout the material and driving the system into a dominant chiral domain state [22]. Thus, the utilization of uncompensated magnetic moment to manipulate AF domain structure, and hence topological spin texture, is critical to the observation of these phenomena.

While Mn_3Sn has only recently been grown in (0001) c-axis-oriented epitaxial thin films [23], cubic Mn_3Ir has been extensively studied in the context of exchange bias, where textured polycrystalline phases [24,25] were shown to yield the largest effects in pinning the reference magnetic electrode in spin valves and MTJs [4,26]. Later developments have proceeded to use Mn_3Ir as the active element in such AF/FM heterostructures, acting as a source of spin current via SHE [27–29] and in turn generating spin-orbit torques [30] resulting in technologically attractive field-free switching of magnetic layers [31,32] desired in high-density MRAM. With such commercial realizations in mind, the use of magnetron sputtering is vital when demonstrating growth of these material systems, due to its speed, flexibility, and scalability (compared with other deposition techniques). Hence, in all

*james.taylor@mpi-halle.mpg.de
†stuart.parkin@mpi-halle.mpg.de

of the above implementations, samples were prepared via sputtering, resulting in polycrystalline thin films of Mn_3Ir.

On the other hand, the elucidation of novel Berry curvature-driven phenomena arising from the triangular spin texture demands test-bed materials with well-controlled crystallographic properties. To reconcile these two requirements, in this work we report the preparation, using magnetron sputtering, of epitaxial thin films of cubic Mn_3Ir with both (001) and (111) orientations. A detailed study of crystal structure shows that high-quality growth can be achieved with sputtering. By comparing our results to those in the literature, we demonstrate the unique performance of the developed deposition procedures. Measurements of the exchange bias induced in heterostructures are used to investigate the magnetic state of the films. To this end, we examine temperature dependence and training effect of exchange bias in epitaxial Mn_3Ir samples, allowing the identification of a crystalline anisotropy to blocking temperature distribution. These results are discussed in the context of topological domain configuration. By highlighting the subtle relationship between exchange bias and crystal microstructure, we underline the importance of its influence when considering noncollinear antiferromagnetic thin films for future chiral spintronic devices.

II. EXPERIMENTAL METHODS

Mn_3Ir thin films were deposited by magnetron sputtering in a BESTEC UHV system with base pressure $<9 \times 10^{-9}$ mbar, using a process Ar gas pressure of 3×10^{-3} mbar. The substrate-target distance was fixed at ≈150 mm, while substrates were rotated to aid homogeneous growth. Thin film samples were grown in both (001) and (111) crystal orientations with various thicknesses, as follows: MgO (001) [substrate]/Mn_3Ir (001) [3 or 10 nm]/TaN [2.5 nm] and Al_2O_3 (0001) [substrate]/TaN (111) [5 nm]/Mn_3Ir (111) [3 or 10 nm]/TaN [2.5 nm]. MgO and Al_2O_3 substrates were ultrasonically cleaned in acetone and ethanol, then clamped mechanically to a holder, and subsequently heated to 250 and 500 °C, respectively, under vacuum for 30 min before deposition.

Mn_3Ir was grown from a $Mn_{80}Ir_{20}$ alloy target, with DC sputtering power of 100 W, resulting in a composition of $Mn_{(0.72\pm0.03)}Ir_{(0.28\pm0.03)}$, that was determined by a combination of Rutherford backscattering spectroscopy (RBS) and energy-dispersive x-ray spectroscopy. As expected from the MnIr phase diagram, and confirmed by later structural measurements, this composition allows the system to form the stoichiometric Mn_3Ir phase with face-centered-cubic (fcc) crystal structure [33]. A TaN capping layer was subsequently grown *in situ* from a Ta target by rf reactive sputtering at 150 W, with 33 vol.% N_2 partial flow introduced to the sputtering gas mixture, resulting in a composition $Ta_{(0.52\pm0.05)}N_{(0.48\pm0.05)}$ as inferred from RBS.

The TaN growth rate was $0.6\,\text{Å}\,\text{s}^{-1}$, while the Mn_3Ir growth rate was $1.2\,\text{Å}\,\text{s}^{-1}$. These were measured using a quartz-crystal microbalance, and deposition times adjusted to obtain desired nominal film thicknesses. Actual thicknesses were subsequently confirmed by measuring x-ray reflectivity (XRR), with fits to the data yielding individual layer thicknesses, as shown in Fig. 1(a). Fringes are observed up to high-reflectivity angles, indicating the growth of smooth films with sharp interfaces. Two thicknesses of Mn_3Ir (3 and 10 nm) were chosen such that their exchange-bias blocking temperatures lie either below or above room temperature, respectively [34].

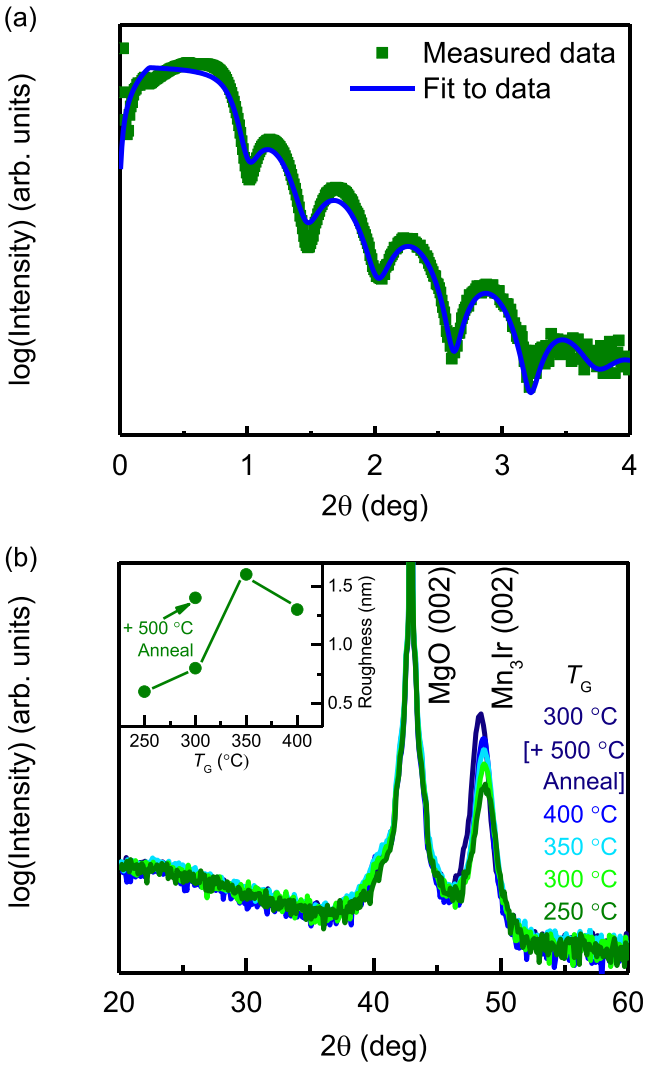

FIG. 1. (a) Measured x-ray reflectivity data from a 10-nm Mn_3Ir (001) film, with fit to determine layer thicknesses. (b) XRD 2θ-θ scans measured for 10-nm Mn_3Ir (001) films grown at different temperatures (inset shows rms roughness measured by AFM for each of these samples).

The films' crystal structure was investigated using a combination of x-ray diffraction (XRD) and transmission electron microscopy (TEM). XRD was performed using a PANalytical X'Pert^3 diffractometer with Cu $K_{\alpha1}$ radiation ($\lambda = 1.5406$ Å). Plane-view high-resolution TEM and cross-sectional high-angle annular dark-field scanning TEM (HAADF-STEM) were measured using an FEI Titan 80–300 microscope, after fabricating thin lamella via focused ion-beam milling.

III. FILM GROWTH AND STRUCTURAL CHARACTERIZATION

Mn_3Ir films with a (001) orientation were achieved by growing on (001) cut single-crystal MgO substrates [35].

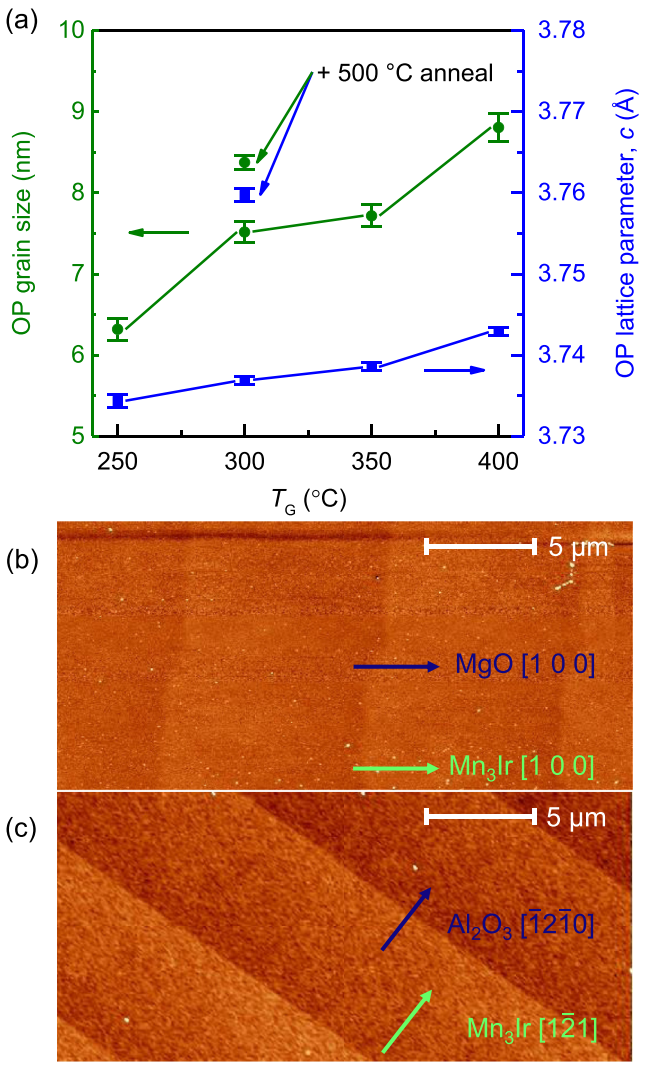

FIG. 2. (a) Dependence of grain size and OP lattice parameter on growth temperature. AFM topography maps of 3-nm Mn_3Ir films with (b) (001) and (c) (111) orientation.

Mn_3Ir was deposited as described above, at different elevated substrate temperatures (growth temperature, T_G). Figure 1(b) shows specular out-of-plane (OP) 2θ-θ XRD patterns for the resulting 10-nm-thick films. In all cases a Mn_3Ir (002) diffraction peak is observed, indicating growth of Mn_3Ir with a (001) crystal orientation. From the full width at half maximum (FWHM) of this peak, the size of crystalline grains in the OP direction can be estimated using the Scherrer formula, as plotted in Fig. 2(a). The intensity of the (002) peak increases with T_G, while its FWHM decreases. This indicates the (001) texture of the film strengthens with increasing T_G, due to the growth of larger grains of consistent crystal orientation. Such a process is further enhanced by *in situ* annealing for 60 min at 500 °C.

The variation of OP lattice parameter, c, is also plotted in Fig. 2(a). As T_G is increased, c relaxes towards the bulk value, presumably because of a combination of the elevated temperature improving adatom mobility and the lower thermal expansion coefficient of the insulating substrate with respect to the metallic film. This process is accentuated by postannealing, after which c approaches the bulk value of 3.780 Å.

The average roughness of the Mn_3Ir layers as a function of growth temperature is plotted in the inset of Fig. 1(b), as measured from atomic force microscopy (AFM) studies. The roughness increases markedly for T_G above 300 °C and after postannealing. As such, subsequent samples were grown at 300 °C without postannealing, to achieve a compromise between high-quality crystal structure and a smooth surface. Under these conditions, $c = (3.737 \pm 0.001)$ Å, remaining slightly below the bulk value. Figure 2(b) shows an AFM topographical map from a 3-nm-thick film grown under such conditions, where terraces of the MgO substrate can be seen stacked along the [100] crystal axis, with the Mn_3Ir following these and showing a low root-mean-square (rms) roughness of ≈8 Å (measured over an area of 25 μm^2). This is in agreement with the roughness parameter of ≈6 Å extracted from fitting XRR measurements.

In this growth mode, Mn_3Ir has a fcc crystal lattice, and can grow in either an $L1_2$ ordered phase ($Pm\bar{3}m$, space group = 221), the crystal and magnetic structure of which is displayed in Fig. 3(a), or a γ disordered phase ($Fm\bar{3}m$, space group = 225) showing site disorder on the respective sublattices [36]. Contrary to previous reports, no (001) superstructure peak from Mn_3Ir is observed in the XRD patterns in Fig. 1(b) [37,38]. Instead, our thin films grow in the γ-Mn_3Ir phase, possessing the noncollinear AF order determined by Kohn *et al.* [36], where the Mn moments have been shown to cant slightly out of the (111) plane.

To evaluate the in-plane (IP) orientation of the Mn_3Ir (001) thin films grown at 300 °C, pole figure XRD measurements were performed in which the azimuthal angle Φ is scanned as a function of tilt angle χ, with 2θ-θ fixed at the (111) reflection of a 10-nm Mn_3Ir (001) film. The [100] and [010] edges of the MgO substrate were aligned along $\phi = 0°$ and $\phi = 90°$, respectively. The resulting map is shown in Fig. 3(b), with the four sharp peaks demonstrating well-defined IP crystal axes arising from a highly oriented thin film with cubic symmetry [37,39]. Furthermore, the peak positions indicate cube-on-cube growth with respect to the MgO substrate, with the epitaxial relationship: MgO (001) [100] ∥ Mn_3Ir (001) [100]. A schematic illustration of this relationship is displayed in Fig. 3(a).

Having determined their IP orientation, 2θ-θ XRD scans (longitudinal direction) at different ω offset angles (transverse direction) were recorded such that the (111) reflections from both the 10-nm Mn_3Ir (001) film and the MgO (001) substrate were observed. Figure 4(a) shows a map of such off-specular ($\theta \neq \omega$) measurements, in which the FWHM of the Mn_3Ir peak in the transverse scans along the ω axis demonstrates a mosaicity ≈2°, comparable with that reported for molecular-beam epitaxy (MBE)-grown films [36]. Table I summarizes the structural parameters obtained for both the (001) and (111) oriented films deposited here, and compares them with results previously reported in the literature. Meanwhile, the FWHM in longitudinal scans along the 2θ axis can be converted to an average crystallite size of (10.6 ± 0.7) nm, comparable with other reports [37]. This contains both IP and OP contributions to grain size suggesting that, since vertical grain size was already determined to be slightly below film

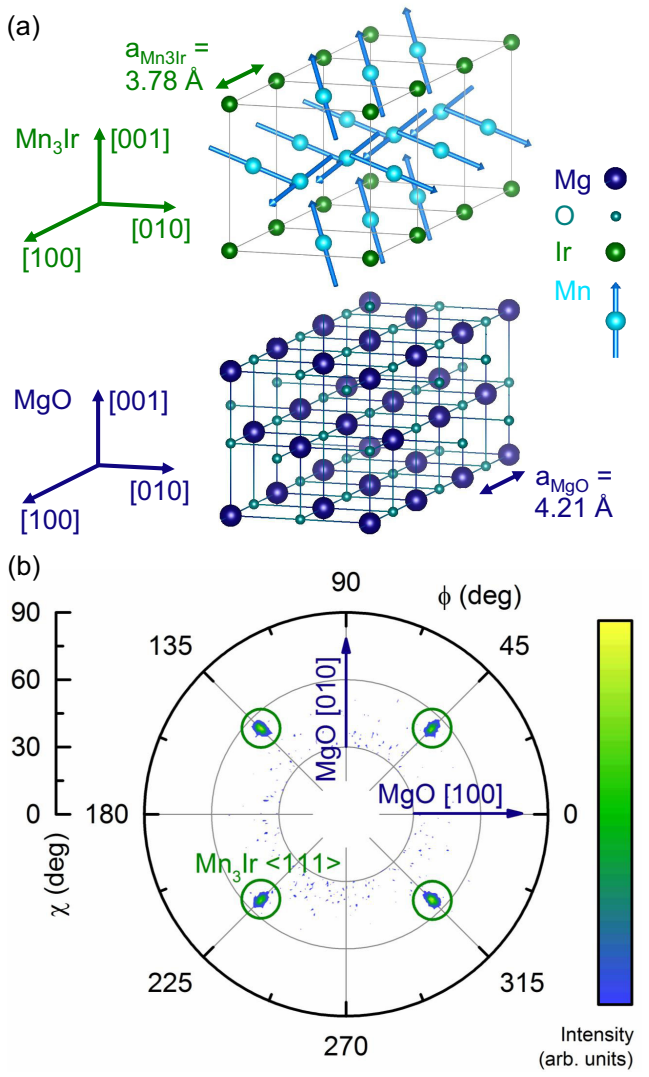

FIG. 3. (a) Crystal and magnetic structure of $L1_2$ ordered Mn_3Ir with [001] axis directed out-of-plane, demonstrating cube-on-cube epitaxy with a (001)-oriented MgO substrate. (b) XRD χ-ϕ pole figure measuring $\langle 111 \rangle$ peaks in a 10-nm Mn_3Ir film with (001) orientation, aligned such that the [100] and [010] axes of the MgO substrate are directed along $\phi = 0^\circ$ and $\phi = 90^\circ$, respectively.

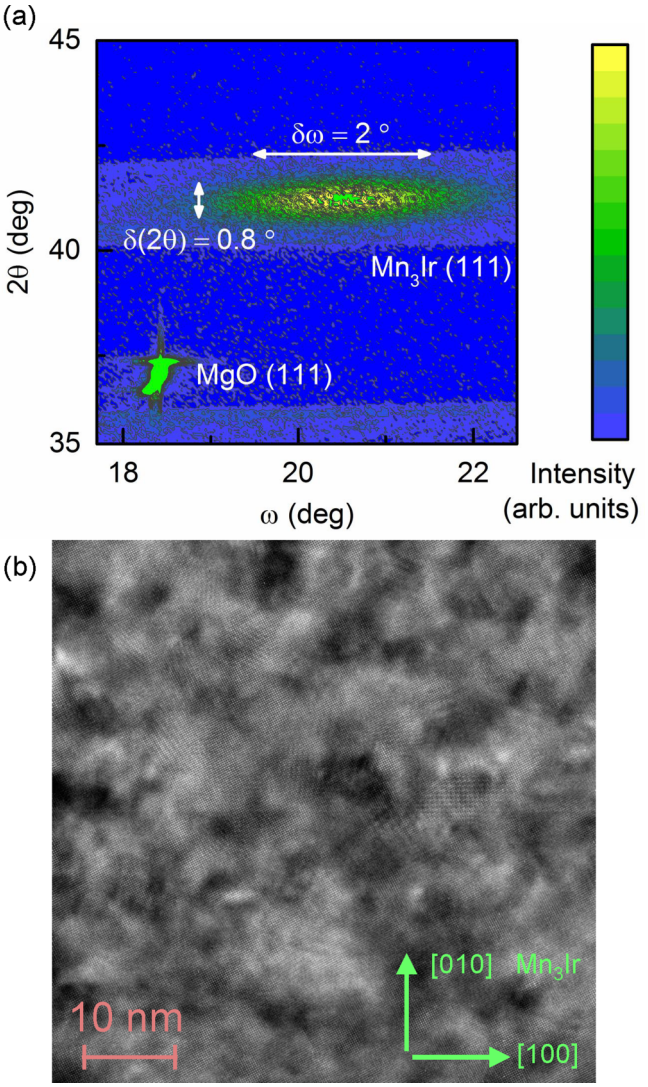

FIG. 4. (a) XRD off-specular scan map measuring (111) reflections from a 10-nm Mn_3Ir film with (001) orientation and the MgO (001) substrate upon which it is grown. (b) Plane-view TEM image of a 3-nm Mn_3Ir (001) thin film, prepared using ion-beam backside thinning.

thickness, crystallites grow larger laterally. This is confirmed by plane-view TEM measurements, displayed in Fig. 4(b). The in-plane microstructure of the sample is visible, with high contrast produced between crystallites with small mosaic spread, showing lateral grain sizes between 10 and 15 nm.

Finally, the IP lattice parameter, a, for a 10-nm Mn_3Ir (001) film grown at 300 °C was calculated to be $a = (3.808 \pm 0.009)$ Å, using the relationship $a = \frac{1}{\sqrt{2}}\sqrt{[(3d_{111})^2 - c^2]}$ [where d_{111} is the interplanar lattice spacing determined from the (111) peak position]. Thus, the film grows with an IP lattice expansion $\varepsilon_\parallel = 0.74\%$, and a corresponding OP lattice contraction $\varepsilon_\perp = -1.14\%$, in agreement with the literature [36]. Due to a large lattice mismatch (≈10%) with MgO (001) ($a = 4.212$ Å), the Mn_3Ir (001) film couples only weakly to the substrate which, while sufficient to seed cube-on-cube growth, will not introduce epitaxial strain. Instead, $\varepsilon_\parallel$ and $\varepsilon_\perp$ can be understood in terms of the film undergoing a small elastic distortion, where unit-cell volume remains almost unchanged with respect to the bulk. We note that mosaicity is increased and lateral grain size suppressed with respect to (111)-orientated films described subsequently. This can be explained by the simultaneous weak substrate-film interaction, combined with the inherent energetic instability of the (001) surface in fcc crystal structures, leading to frequent relaxation of the slight tetragonal distortion in Mn_3Ir, creating a higher areal density of grain boundaries and an enhanced rotation between neighboring grains.

Moving on to the characterization of Mn_3Ir thin films with a (111) orientation deposited on Al_2O_3 (0001) substrates ($a = 4.759$ Å), in this case γ-Mn_3Ir grows with the same fcc structure, but with the (111) crystal planes lying in the film plane in registry with the hexagonal substrate. Figure 5(a) shows

TABLE I. Summary of crystal-structure parameters indicative of high-quality thin films, comparing the superior quality growth achieved in this work with previously published results discussed in the main text. Magnitude of exchange-bias fields reported for different heterostructure configurations, as well as the resulting interfacial exchange anisotropy energy densities, are also quoted alongside the thickness of the Mn_3Ir film utilized and the temperature of the measurement.

Growth technique	Material system	Lattice parameter (Å)	Mosaic spread (°)	Grain size (nm)	Exchange bias field, $\mu_0 H_{EB}$ (mT)	Exchange anisotropy energy density, J_K (erg cm^{-2})
Magnetron sputtering [this work]	γ-Mn_3Ir (001) [/NiFe]	c, 3.737 ± 0.001 a, 3.808 ± 0.009	2	OP: 7.5 IP: 10–15	28 (10 nm@RT) 121 (3 nm@5 K with $\mu_0 H_{FC} \parallel$ [110]) 104 (3 nm@5 K with $\mu_0 H_{FC} \parallel$ [100]) 77 (3 nm@5 K with $\mu_0 H_{FC} \parallel$ [100] after training)	0.107 (10 nm@RT) 0.462 (3 nm@5 K with $\mu_0 H_{FC} \parallel$ [110]) 0.397 (3 nm@5 K with $\mu_0 H_{FC} \parallel$ [100]) 0.294 (3 nm@5 K with $\mu_0 H_{FC} \parallel$ [100] after training)
	γ-Mn_3Ir (111) [/NiFe]	c, 3.797 ± 0.001 a, 3.84 ± 0.08	0.5	OP: 10.1 IP: 20	29 (10 nm@RT) 95 (3 nm@5 K) 27 (3 nm@5 K after training)	0.115 (10 nm@RT) 0.361 (3 nm@5 K) 0.103 (3 nm@5 K after training)
MBE [37]	[Fe (001)/] γ-Mn_3Ir (001)	a, 3.79 ± 0.05	6	10	4 (10 nm@RT)	
MBE [36]	[Fe (001)/] γ-Mn_3Ir (001)	c, 3.736 ± 0.008 a, 3.80	2		6 (15 nm@RT)	0.07 (15 nm@RT)
	$L1_2$-Mn_3Ir (001) [/Fe (001)]	c, 3.725 ± 0.005 a, 3.81			31 (15 nm@RT)	0.37 (15 nm@RT)
Magnetron sputtering [38]	$L1_2$-Mn_3Ir (111)	c, 3.78 a, 3.80	2.8	15		
Magnetron sputtering [59,60]	$L1_2$-Mn_3Ir (111) [/CoFe]			8.5	≈200 mT (10 nm@RT)	1.3 (10 nm@RT)
Magnetron sputtering [39]	γ-Mn_3Ir (001) [/CoFe]			OP :≈ 10 IP: >20		≈0.2 (10 nm@RT)
	γ-Mn_3Ir (111) [/CoFe]					≈0.35 (10 nm@RT)
	γ-Mn_3Ir (poly) [/CoFe]					≈0.45 (10 nm@RT)
Magnetron sputtering [25]	γ-Mn_3Ir (poly) [/CoFe]			6	≈42 mT (9 nm@RT)	
				12	≈35 mT (9 nm@RT)	
				≈6	≈40 mT (3 nm@ ≈ 5 K)	
Magnetron sputtering [46]	γ-Mn_3Ir (poly) [/CoFe]				≈8 mT	

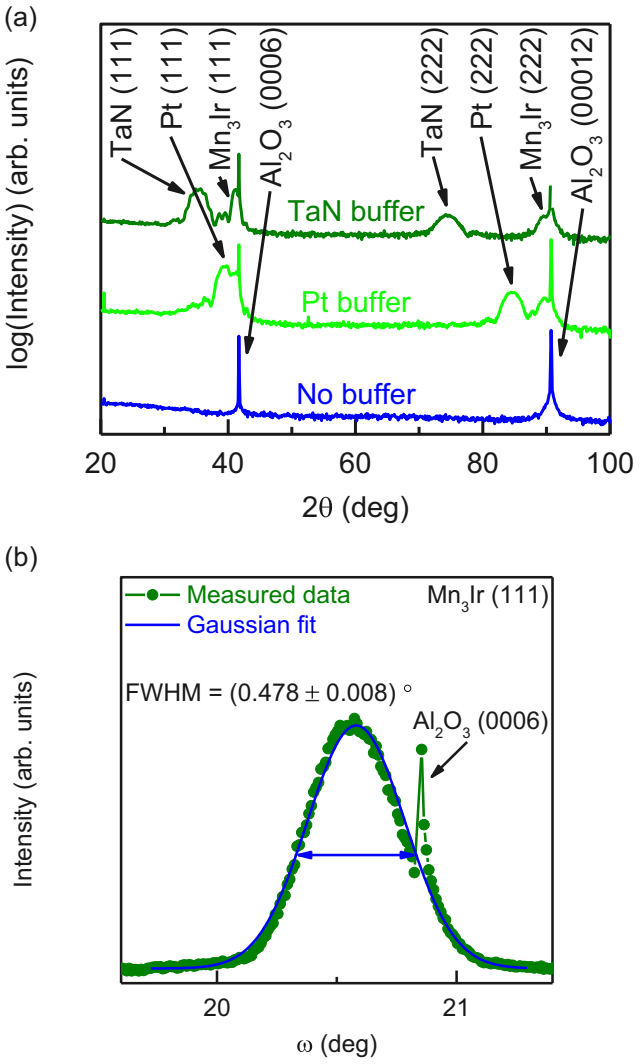

FIG. 5. (a) XRD 2θ-θ patterns measured for 10-nm Mn_3Ir (111) films grown using different buffer layers (scans are offset for clarity). (b) XRD ω rocking curve for a 10-nm Mn_3Ir (111) film grown on a TaN buffer layer, with fit to determine FWHM.

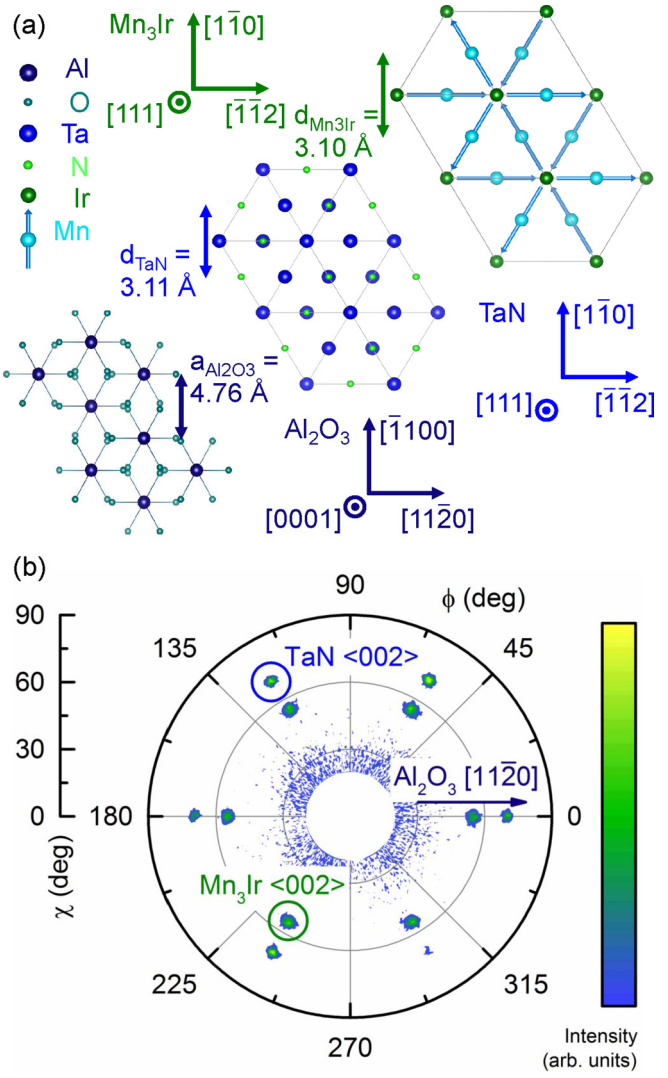

FIG. 6. (a) Crystal and magnetic structure of (111) planes in $L1_2$ ordered Mn_3Ir, of (111) planes in TaN and of (0001) planes in Al_2O_3, showing the epitaxial relation between them as viewed along the OP axis. (b) XRD χ-ϕ pole figure measuring $\langle 002 \rangle$ peaks in a 10-nm Mn_3Ir film with (111) orientation and a 5-nm TaN (111) buffer layer, aligned such that the [11$\bar{2}$0] axis of the Al_2O_3 substrate is directed along $\phi = 0^\circ$.

specular OP 2θ-θ XRD patterns for 10-nm Mn_3Ir films grown according to the previously discussed conditions, but now utilizing various buffer layers. In the case where Mn_3Ir is grown directly on Al_2O_3 (0001), no crystalline structure is observed. This can be explained by a significant variation in interface free energies between the Al_2O_3 (0001) and Mn_3Ir (111) surfaces making this growth mode unfavorable [40], a difference that may be reduced by the introduction of a buffer layer.

Therefore, two different buffer layers were employed; either 5-nm Pt or 5-nm TaN was deposited on Al_2O_3 substrates held at 500 °C. TaN was prepared according to the conditions described above, while Pt was deposited using a DC sputtering power of 50 W at a rate of 1.0 Å s^{-1}. Intense (111) and (222) peaks arising from both Pt and TaN are observed in Fig. 5(a), indicating that both films grow epitaxially on the hexagonal substrate with a sharp (111) texture [41]. Furthermore, both buffer layers seed a (111) orientation into the subsequently deposited 10-nm Mn_3Ir. A TaN buffer was chosen for further samples, giving the advantages of chemical stability, a smooth surface (with rms roughness of <3 Å confirmed by AFM), and a high resistance (measured as >2 mΩ cm via a four-probe method, in agreement with literature values [42]). From the OP 2θ-θ XRD pattern in Fig. 5(a), a lattice parameter for TaN of (4.397 ± 0.004) Å is measured, which is close to the value for relaxed TaN thin films of 4.383 Å [42].

A lattice parameter value of (3.797 ± 0.001) Å is deduced for Mn_3Ir (111). This is very close to the bulk value, indicating that the film grows fully relaxed, in agreement with sputtered films prepared by Jara *et al.* [38]. OP grain size is calculated via the Scherrer formula to be (10.1 ± 0.3) nm, again demonstrating the correlation of grain size vertically with film thickness. A low mosaic spread in the film is measured as (0.478 ± 0.008)° by recording a ω rocking curve XRD scan about the Mn_3Ir (111) peak, displayed in Fig. 5(b). This low mosaicity, alongside the high-quality (111) crystal

structure, can be attributed to the small lattice mismatch when using a TaN buffer layer, allowing relaxed film growth with minimal introduction of misfit dislocations or other defects. Indeed, between two periods of the Al_2O_3 substrate lattice and three of the TaN buffer, the lattice mismatch amounts to 2.0%, which in turn reduces to just 0.3% between the (111)-oriented TaN and the kagome planes of Mn atoms, based on measured lattice parameters. The rms roughness of the films is <4 Å, as extracted from Fig. 2(c), where the step and terrace topography of the Al_2O_3 substrate is observed via AFM through a 3-nm Mn_3Ir (111) film.

Based on this analysis of lattice mismatch, Fig. 6(a) displays the expected IP orientation of the stack, alongside experimentally determined lattice parameters. This mode of epitaxial growth was confirmed by XRD pole figures, presented in Fig. 6(b), measuring the (002) reflections of (111)-oriented TaN and Mn_3Ir when the $[11\bar{2}0]$ axis of the substrate was aligned along $\phi = 0^\circ$. The sharp peaks observed provide evidence of coherent IP crystallographic directions, while their sixfold symmetry suggests rotational twinning between (111) crystal planes [38,39]. The relative positions of the reflections confirm pseudo-hexagon-on-hexagon epitaxial growth throughout the stack, and allow the determination of the following epitaxial relationship, illustrated in Fig. 6(a): Al_2O_3 (0001) $[11\bar{2}0]$ $[\bar{1}100] \parallel$ TaN(111) $[\bar{1}\bar{1}2]$ $[1\bar{1}0] \parallel Mn_3Ir(111)$ $[\bar{1}\bar{1}2]$ $[1\bar{1}0]$.

Additional TEM measurements on the (111)-oriented samples investigated the film structure at the nanoscale. A cross-section HAADF-STEM image of a 10-nm Mn_3Ir film is displayed in Fig. 7(a), viewed along the $[1\bar{1}0]$ zone axis. The epitaxial growth of the TaN (111) buffer and Mn_3Ir (111) film is clearly seen, demonstrating high-quality crystal structure with sharp interfaces and few defects. An absence of grain boundaries observed within the field of view suggests growth of large grains in the lateral direction, with a size of >20 nm.

Figure 7(b) shows a fast Fourier transform diffractogram of the lattice plane image in Fig. 7(a), with (*hkl*) diffraction peaks indexed. The positions of the diffraction spots confirm the epitaxial relationship between the layers. They further allow the determination of the predominantly IP lattice parameter along the [001] direction: (4.35 ± 0.09) Å for TaN and (3.84 ± 0.08) Å for Mn_3Ir. These agree, within uncertainty, with the OP lattice parameters measured from XRD, confirming the relaxed growth of Mn_3Ir (111). Table I collates the different crystal-structure figures of merit measured for our thin films, demonstrating the competitive performance of the magnetron sputtering growth protocols developed here with those previously published.

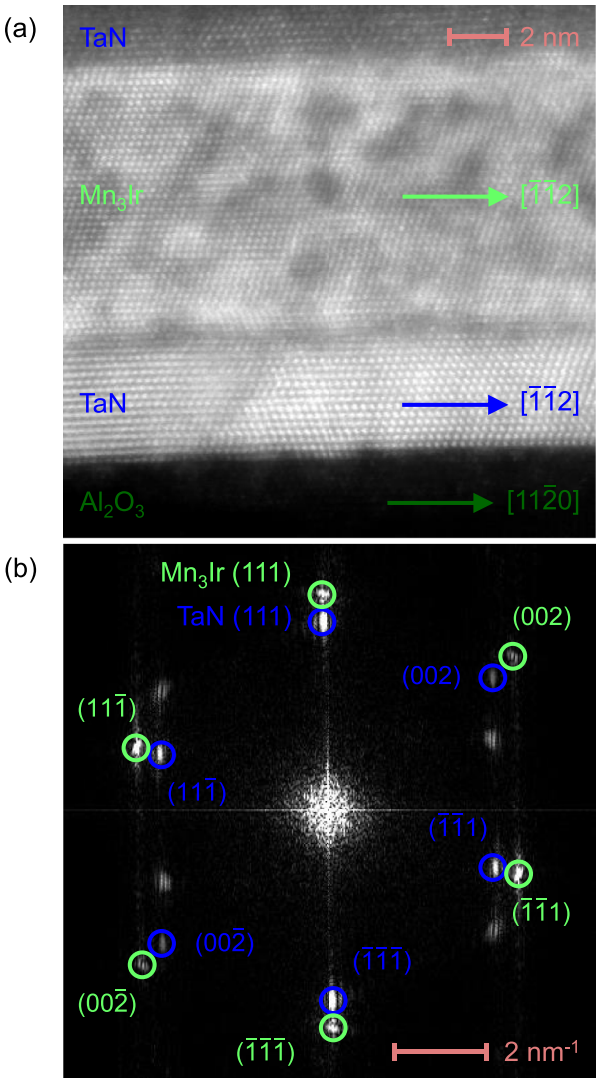

FIG. 7. (a) Cross-sectional HAADF-STEM image of a 10-nm Mn_3Ir (111) film, grown on an Al_2O_3 substrate with (0001) orientation using a 5-nm (111) textured TaN buffer layer, viewed along the $[1\bar{1}0]$ zone axis. (b) Diffractogram (fast Fourier transform) of the above experimental image. The epitaxial correlation between the Mn_3Ir and TaN lattices is demonstrated by the corresponding indexed reflections.

IV. EXCHANGE BIAS

Exchange bias (EB) was studied in bilayer samples of Mn_3Ir/FM. To achieve this, replicas of the above samples were prepared incorporating a layer of 5 nm $Ni_{80}Fe_{20}$ (=Py, Permalloy), grown from a $Ni_{80}Fe_{20}$ alloy target at a rate of 1.2 Å s^{-1} via 75-W DC magnetron sputtering after samples had cooled to room temperature (RT), resulting in the growth of polycrystalline Py with composition $Ni_{(0.80\pm0.01)}Fe_{(0.20\pm0.01)}$ (measured by RBS). The magnetic properties of the resulting heterostructures were measured using superconducting quantum interference device vibrating sample magnetometry (Quantum Design MPMS3).

EB occurs in coupled AF/FM systems, introducing a unidirectional anisotropy to the bilayer. This manifests itself as a shift in the FM magnetization hysteresis loop along the applied field axis, the exchange-bias field ($\mu_0 H_{EB}$), as well as an enhancement of coercive field ($\mu_0 H_C$) [43,44]. EB is generally regarded as resulting from uncompensated spins at the interface of the AF [45,46], which exchange couple to moments in the FM layer [47,48]. These uncompensated AF spins are, in turn, strongly pinned in the direction of unidirectional anisotropy by AF domains that extend into the bulk of the film [49,50]. EB is set in a given direction at sufficient temperatures to overcome an energy barrier to AF domain reorientation, namely the blocking temperature, T_B. Here the application of an external magnetic field that saturates the FM

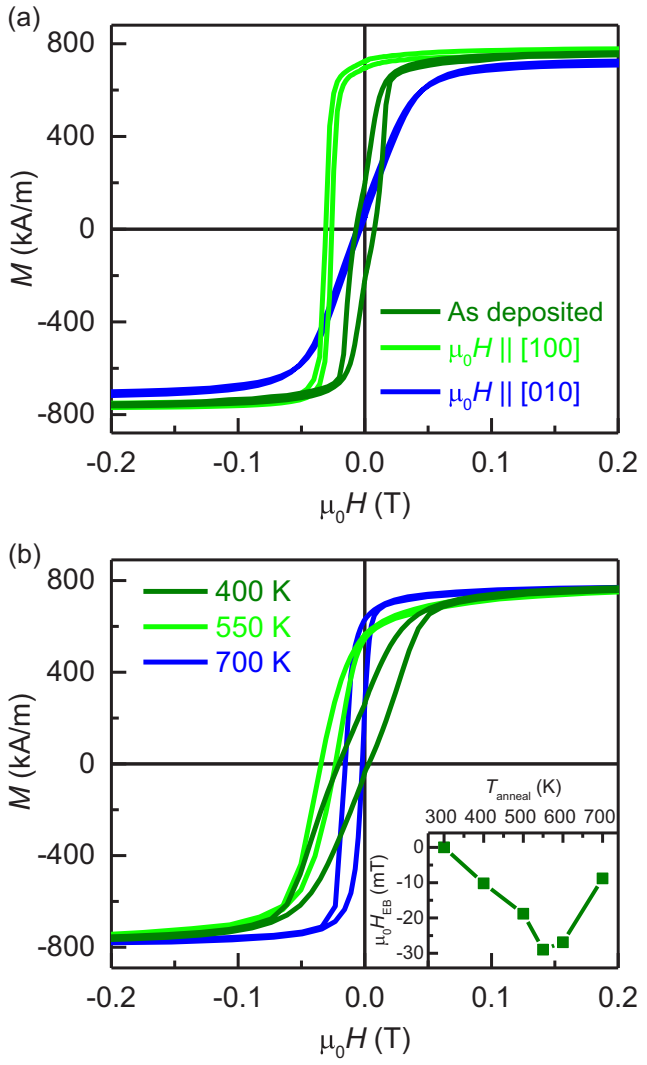

FIG. 8. (a) Magnetization hysteresis loops at 300 K for an as-deposited 10-nm Mn_3Ir (001)/Py bilayer, and for the same sample after 1-T IP field annealing at 550 K (with $\mu_0 H_{FA} \parallel [100]$), with IP measurement field directed parallel and perpendicular to $\mu_0 H_{FA}$. (b) Magnetization hysteresis loops at 300 K for a 10-nm Mn_3Ir (111)/Py bilayer after 1-T IP field annealing at different temperatures (with $\mu_0 H_{FA} \parallel [\bar{1}\bar{1}2]$) (inset shows variation of $\mu_0 H_{EB}$ with annealing temperature).

will also align the coupled uncompensated moments, in turn leading to coherent orientation of bulk AF domains [51,52]. As the heterostructure is cooled, the preferential AF domain alignment becomes fixed below T_B and exchange anisotropy is set in the direction of the external field [49,50]. The various characteristics of EB are determined by the thermal stability of the resulting AF domain walls, and hence depend intimately on film microstructure [53,54].

For the case of 10-nm Mn_3Ir/Py bilayers, T_B lies above 300 K, meaning an EB can be stabilized at RT [24]. Figure 8(a) shows magnetization (M) measured as a function of IP field ($\mu_0 H$) for a 10-nm Mn_3Ir (001)/Py bilayer; both as-deposited and after 30-min magnetic-field annealing (FA) at 550 K and subsequent cooling in a 1-T magnetic field ($\mu_0 H_{FA}$) applied along the [100] crystal direction (performed *ex situ* in a furnace at a pressure $<9 \times 10^{-6}$ mbar). The field annealing procedure did not result in modification of the crystal structure of the bilayer, as confirmed by XRD measurements. In the as-deposited state, no shift in the magnetization hysteresis (MH) loop can be seen. Following the IP field-annealing procedure, a shift in the MH loop of $\mu_0 H_{EB} = -28$ mT, measured with applied field along the [100] axis in Mn_3Ir, demonstrates the onset of EB. This value of $\mu_0 H_{EB}$ is equivalent to a unidirectional anisotropy energy density (defined as $J_K = M_S d_F \mu_0 H_{EB}$, where M_S is the saturation magnetization and d_F is the thickness of the FM layer [55]) of $J_K = 0.107\,\mathrm{erg\,cm^{-2}}$ (in turn equivalent to $10.7\,\mathrm{nJ\,cm^{-2}}$). Magnetization measured with external field along the perpendicular [010] crystallographic direction shows a hard axis response, confirming the unidirectional nature of the induced anisotropy. The negative shift of the hysteresis loops indicates the exchange anisotropy is set in the same direction as the field applied during annealing. This is because of the parallel coupling between interfacial Mn spins and Ni magnetic moments, which is shown to dominate over antiparallel coupling with Fe when smoothly varying Py to a Ni-rich composition [56]. These uncompensated AF moments become, in turn, strongly pinned in their preferred direction by the dominant AF domain state in the bulk of the Mn_3Ir film as the sample is cooled through T_B [55].

Figure 8(b) shows MH loops measured for a 10-nm Mn_3Ir (111)/Py heterostructure with field applied along the $[\bar{1}\bar{1}2]$ crystalline direction after 30-min *ex situ* 1-T IP field annealing at different temperatures, T_{anneal}. In all cases, a negative shift of the hysteresis loop indicates the introduction of a unidirectional exchange anisotropy. The inset of Fig. 8(b) shows the variation in $\mu_0 H_{EB}$ with T_{anneal}. A maximum $\mu_0 H_{EB} = -29$ mT is achieved after IP FA at 550 K, corresponding to a unidirectional anisotropy energy density of $J_K = 0.115\,\mathrm{erg\,cm^{-2}}$ ($J_K = 11.5\,\mathrm{nJ\,cm^{-2}}$). Higher annealing temperatures lead to a degradation of $\mu_0 H_{EB}$, indicating that T_B of these bilayers is close to 550 K, comparable to other values for epitaxially grown Mn_3Ir films in the literature [35]. Contrary to Ref. [39], where larger $\mu_0 H_{EB}$ is measured for (111) textured films of similar thickness, we find similar $\mu_0 H_{EB}$ for both Mn_3Ir orientations. In our case, larger than expected $\mu_0 H_{EB}$ for (001)-orientated films may be explained by these samples containing a higher density of grain boundaries and larger mosaicity compared with the (111) films, as discussed above, which may act to enhance EB by introducing pinning sites to stabilize AF domain formation [57].

Table I compares EB values achieved in these bilayers with optimized $\mu_0 H_{EB}$ and J_K previously reported. The $\mu_0 H_{EB}$ and J_K values achieved here compare favorably with other epitaxially grown films, also reinforcing the assertion that our Mn_3Ir thin films possess a noncollinear AF order (since EB is shown to degrade significantly when transitioning towards the collinear AF phase of $Mn_{50}Ir_{50}$ [58]). Nevertheless, for both orientations we measure lower $\mu_0 H_{EB}$ and J_K compared to maximized values in the literature. This is because larger values of $\mu_0 H_{EB}$ and J_K are obtained in textured polycrystalline films containing much smaller grains (thus more pinning sites) [25] and a fraction of $L1_2$ ordered Mn_3Ir phase [59,60].

On the other hand, the T_B of 3 nm Mn_3Ir/Py bilayers will lie below RT. It has been shown that T_B decreases rapidly when

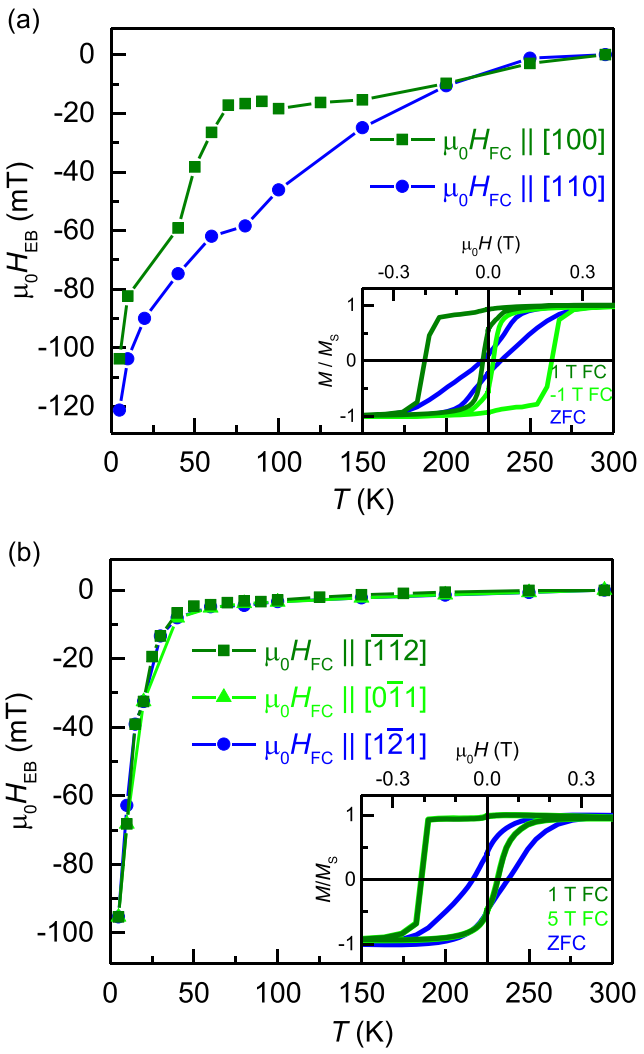

FIG. 9. (a) $\mu_0 H_{EB}$ measured at different temperatures after 1-T IP field cooling from 400 K for a 3-nm Mn_3Ir (001)/Py bilayer, with $\mu_0 H_{FC} \parallel [100]$ and [110] crystal axes (inset shows normalized magnetization hysteresis loops recorded at 5 K after different field-cooling protocols with $\mu_0 H_{FC} \parallel [100]$). (b) $\mu_0 H_{EB}$ measured at different temperatures after 1-T IP field cooling from 400 K for a 3-nm Mn_3Ir (111)/Py bilayer, with $\mu_0 H_{FC} \parallel [\bar{1}\bar{1}2]$, $[0\bar{1}1]$, and $[1\bar{2}1]$ crystal axes (inset shows normalized magnetization hysteresis loops recorded at 5 K after different field-cooling protocols with $\mu_0 H_{FC} \parallel [\bar{1}\bar{1}2]$).

Mn_3Ir thickness is reduced below 5 nm [24,57] due to the reduced thermal stability of the AF domain state [61]. However, no studies of EB in ultrathin epitaxial Mn_3Ir films have previously been reported. Figure 9(a) shows the value of $\mu_0 H_{EB}$ measured for such a bilayer with (001) orientation after 1 T IP field cooling (FC) from 400 K to different temperatures, T. The inset to Fig. 9(a) shows an example of the individual MH loops measured at 5 K after zero-field cooling (ZFC), +1-T IP field cooling and −1-T IP field cooling. Shifting of the MH loop along the applied field axis after field cooling, as opposed to ZFC, indicates the onset of EB at low temperatures and demonstrates the essential role of the external field ($\mu_0 H_{FC}$) in selecting a preferred direction for interfacial AF spins. The reversal of the unidirectional anisotropy after −1-T field cooling confirms the parallel coupling of the uncompensated Mn and FM Ni moments, while also showing the ability to manipulate interfacial magnetic structure and AF domain orientation as a function of field cooling.

Figure 9(a) also shows the change in $\mu_0 H_{EB}$ when exchange anisotropy is induced by cooling the sample (and subsequently measuring) with magnetic field applied along different crystallographic directions. An onset of $\mu_0 H_{EB}$ increase indicates T_B of the heterostructures. With EB along the [110] crystal axis, a higher $T_B \approx 150$ K is observed compared with the [100] axis ($T_B \approx 60$ K), as well as larger values of $\mu_0 H_{EB}$ at equivalent temperatures, in agreement with Ref. [35]. There is no obvious relation between microstructure (e.g., film terrace orientation measured by AFM) and this preferential axis for unidirectional anisotropy. However, an epitaxial AF layer can imprint its magnetocrystalline anisotropy onto a polycrystalline FM layer in exchange-coupled heterostructures [62]. EB phenomena are then governed by a combination of unidirectional exchange anisotropy set through field cooling, and an anisotropy determined by the AF crystal symmetry. In our case, the enhanced T_B along the [110] direction may be caused by a different magnetocrystalline anisotropy compared with the [100] axis, in turn connected to the alignment of Mn moments in the γ-Mn_3Ir structure at 45° to the cubic crystallographic edges. The triangular spin texture of epitaxial Mn_3Ir films has been shown to have a significant influence on the magnetization reversal mechanism in AF/FM bilayers [36], and, while the relationship between $\mu_0 H_{EB}$ and magnetocrystalline easy axes of epitaxial FM layers has been studied [63], the effect of crystalline anisotropy in noncollinear AF films on EB is open to further exploration.

The measurement of $\mu_0 H_{EB}$ in a 3-nm Mn_3Ir (111)/Py bilayer at different temperatures after 1-T IP field cooling from 400 K is shown in Fig. 9(b). In this case, no difference is seen in $\mu_0 H_{EB}$ with cooling field applied along different crystal directions. This may be due to sixfold IP crystalline symmetry in these samples, such that no direction provides a preferential axis for EB setting. Observed $T_B \approx 40$ K is found to be lower than (001)-oriented Mn_3Ir, as is $\mu_0 H_{EB}$ at equivalent temperatures, with maximum $\mu_0 H_{EB} = -95$ mT at 5 K. Again, this may be attributable to higher-quality epitaxial growth of (111) films, introducing less defects and grain boundaries to stabilize AF domains at a given temperature [57].

The inset of Fig. 9(b) shows individual MH loops recorded at 5 K following IP field cooling with different external field strengths. The asymmetric shape of the hysteresis loops indicates that the magnetization of the Py layer reverses via the same two distinct mechanisms, domain-wall nucleation/propagation on the downward sweep of magnetic field and coherent magnetization rotation on the recoil branch, as previously discovered for Mn_3Ir [64]. In addition, $\mu_0 H_{EB}$ is invariant with field strength as expected, again indicating the potential uses of EB in manipulating AF order using low applied fields. Indeed, EB may play a valuable role when utilizing chiral AFs for spintronic applications, by setting a dominant domain state in a material [51] with otherwise large internal anisotropy fields, when the uncompensated moment induced at the interface [48] acts to coherently orient triangular spin configuration. Extending this concept to materi-

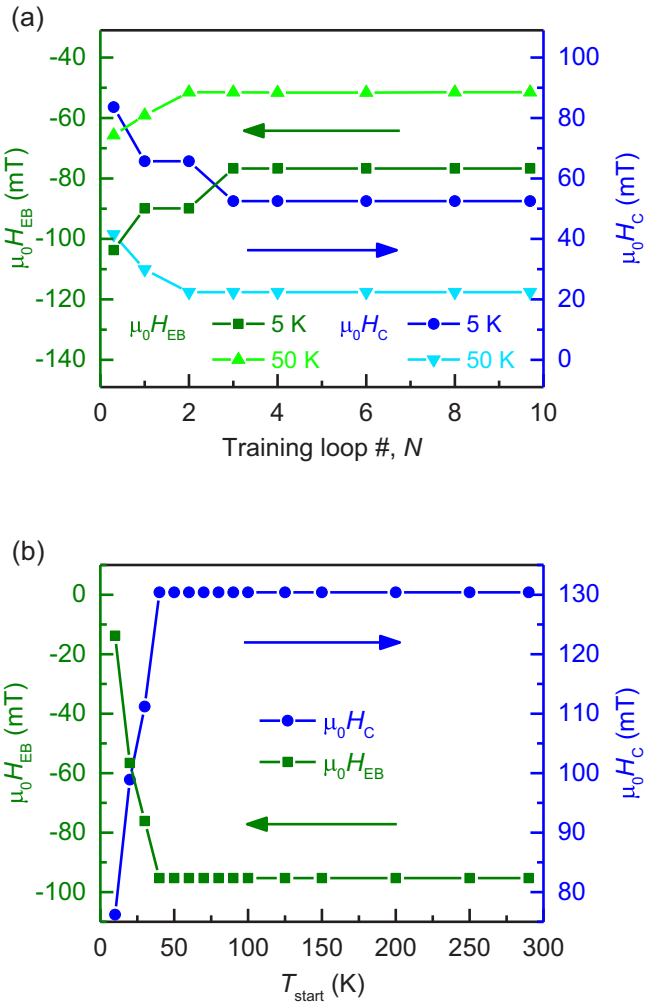

FIG. 10. (a) Exchange-bias training effect showing variation of $\mu_0 H_{EB}$ and $\mu_0 H_C$ with successive measurement field cycles at different temperatures after 1-T IP field cooling from 300 K for a 3-nm Mn_3Ir (001)/Py bilayer (with $\mu_0 H_{FC} \parallel [100]$). (b) Blocking temperature distribution showing $\mu_0 H_{EB}$ and $\mu_0 H_C$ measured at 5 K after 1-T IP FC from different starting temperatures for a 3-nm Mn_3Ir (111)/Py bilayer (with $\mu_0 H_{FC} \parallel [\bar{1}\bar{1}2]$).

als such as Mn_3Sn [20], where weak magnetization can be used to directly manipulate chiral domain orientation [22], exchange interactions across heterostructures of epitaxially grown noncollinear AF films could be used to control topological spin textures. AF domains in Mn_3Ir, and their relation to uncompensated moment, are considered in our subsequent work [65].

For such realizations, an important consideration is the EB training effect. Here the measured $\mu_0 H_{EB}$ and $\mu_0 H_C$ decrease over the course of successive external applied magnetic-field cycles. This arises because a portion of the uncompensated AF moments at the interface, that contribute to exchange coupling after the initial field-cooling procedure, are only weakly pinned to the bulk AF structure. They are thus free to follow the reversing magnetization of the FM layer, and so are reorientated by the external field [45]. In Fig. 10(a) the change in $\mu_0 H_{EB}$ and $\mu_0 H_C$ measured over the course of consecutive training-field cycles is shown for a (001)-oriented 3-nm Mn_3Ir/Py bilayer, following 1-T IP field cooling from 300 K to different temperatures. In all cases, it is observed that, after at most four applied field cycles, both $\mu_0 H_{EB}$ and $\mu_0 H_C$ reach equilibrium values and do not change further. At this point all weakly pinned uncompensated Mn spins are relaxed. The remaining exchange bias is modulated by interfacial AF spins that are strongly coupled to the bulk Mn_3Ir domain state [48]. Similar results are seen for 3-nm Mn_3Ir (111)/Py heterostructures (not shown).

These resulting values of exchange bias therefore depend on the stability of the AF order, and hence on the temperature to which the bilayer was field cooled. While before training both Mn_3Ir orientations show large $\mu_0 H_{EB} \geqslant -95$ mT at 5 K, the maximum post-training $\mu_0 H_{EB} = -77$ mT for a 3-nm Mn_3Ir (001)/Py bilayer and $\mu_0 H_{EB} = -27$ mT for the (111) orientation. The dramatic decrease in $\mu_0 H_{EB}$ for the 3-nm Mn_3Ir (111)/Py bilayer may indicate the significant contribution to the initial exchange-bias setting of weakly coupled uncompensated Mn moments in ultrathin films of this orientation, as discussed further in our subsequent work [65].

Finally, in order to confirm the T_B of bilayers with ultrathin Mn_3Ir, further temperature-dependent measurements of exchange bias were performed. In Fig. 10(b) the variation in $\mu_0 H_{EB}$ and $\mu_0 H_C$, extracted from magnetization hysteresis loops measured at 5 K after 1-T IP field cooling from different starting temperatures, T_{start}, is shown for a 3-nm Mn_3Ir/Py bilayer with (111) orientation. A sharp decrease in both $\mu_0 H_{EB}$ and $\mu_0 H_C$ is observed when cooling from temperatures below 40 K, indicating that T_{start} is no longer completely above the maximum of the bilayer's T_B distribution, and thus insufficiently energetic to fully reorient AF domains in order to obtain maximum exchange bias. Variation in grain size within the Mn_3Ir film results in a distribution of these activation energies and hence of T_B, accounting for the steady decrease in $\mu_0 H_{EB}$ towards zero as T_{start} is further decreased [25].

V. CONCLUSION

In summary, recipes for the sputter deposition of γ-Mn_3Ir with (001) orientation on MgO substrates, and with (111) orientation on TaN buffered Al_2O_3 substrates, are reported. A combination of XRD and TEM analysis demonstrates the epitaxial growth of the films and the resulting high-quality crystal structure, with Mn_3Ir (111) films in particular showing low mosaicity and large grain size. The ability to manipulate crystal texture through epitaxial engineering, while achieving single-crystalline thin-film structure using magnetron sputtering, represents an important springboard for exploiting epitaxial thin films of Mn_3Ir and other chiral antiferromagnets in topological spintronic applications.

Exchange bias was studied in bilayer samples, with values up to $\mu_0 H_{EB} = -29$ mT ($J_K = 0.115$ erg cm^{-2} or 11.5 nJ cm^{-2}) achieved after 1-T in-plane field annealing at 550 K. For heterostructures with ultrathin epitaxial antiferromagnetic layers, the temperature dependence of exchange bias is studied. Exchange bias is observed below room temperature, with $T_B \approx 40$ K in 3-nm Mn_3Ir (111)/Py samples

and a notable dependence of exchange coupling on in-plane crystalline direction in 3-nm Mn_3Ir (001)/Py bilayers. Here a higher $T_B \approx 150$ K and larger values of $\mu_0 H_{EB}$ are measured when unidirectional anisotropy is set along the [110] crystallographic axis. These findings may inform future studies of spin-orbit torques in such heterostructures.

Finally, we explore how these macroscopic exchange-bias properties provide a clue as to the underlying antiferromagnetic domain structure, based on the domain-state model. By discussing exchange anisotropy in the context of our detailed analysis of crystal microstructure, this paper provides groundwork as to how exchange coupling might be used to control triangular spin textures in heterostructures of noncollinear antiferromagnets utilized in *chiralitronic* devices.

ACKNOWLEDGMENTS

We acknowledge Dr. Andrew Kellock for RBS measurements, and Dr. Holger L. Meyerheim for assistance with XRD analysis. We thank Prof. Gernot Güntherodt for helpful discussion. This work was partially funded by ASPIN (EU H2020 FET Open Grant No. 766566).

[1] S. S. P. Parkin, N. More, and K. P. Roche, Phys. Rev. Lett. **64**, 2304 (1990).
[2] S. S. P. Parkin and D. Mauri, Phys. Rev. B **44**, 7131 (1991).
[3] S. S. P. Parkin, J. Xin, C. Kaiser, A. Panchula, K. Roche, and M. Samant, Proc. IEEE **91**, 661 (2003).
[4] S. S. P. Parkin, K. P. Roche, M. G. Samant, P. M. Rice, R. B. Beyers, R. E. Scheuerlein, E. J. O'Sullivan, S. L. Brown, J. Bucchigano, D. W. Abraham, Y. Lu, M. Rooks, P. L. Trouilloud, R. A. Wanner, and W. J. Gallagher, J. Appl. Phys. **85**, 5828 (1999).
[5] S. H. Yang, K. S. Ryu, and S. S. P. Parkin, Nat. Nanotechnol. **10**, 221 (2015).
[6] S. S. P. Parkin, M. Hayashi, and L. Thomas, Science **320**, 190 (2008).
[7] K. S. Ryu, L. Thomas, S. H. Yang, and S. S. P. Parkin, Nat. Nanotechnol. **8**, 527 (2013).
[8] A. J. Sievers and M. Tinkham, Phys. Rev. **129**, 1566 (1963).
[9] V. Baltz, A. Manchon, M. Tsoi, T. Moriyama, T. Ono, and Y. Tserkovnyak, Rev. Mod. Phys. **90**, 015005 (2018).
[10] P. Wadley, B. Howells, J. Železný, C. Andrews, V. Hills, R. P. Campion, V. Novák, K. Olejník, F. Maccherozzi, S. S. Dhesi, S. Y. Martin, T. Wagner, J. Wunderlich, F. Freimuth, Y. Mokrousov, J. Kuneš, J. S. Chauhan, M. J. Grzybowski, A. W. Rushforth, K. W. Edmonds, B. L. Gallagher, and T. Jungwirth, Science **351**, 587 (2016).
[11] S. Y. Bodnar, L. Šmejkal, I. Turek, T. Jungwirth, O. Gomonay, J. Sinova, A. A. Sapozhnik, H. J. Elmers, M. Kläui, and M. Jourdan, Nat. Commun. **9**, 348 (2018).
[12] D. Kriegner, K. Výborný, K. Olejník, H. Reichlová, V. Novák, X. Marti, J. Gazquez, V. Saidl, P. Němec, V. V. Volobuev, G. Springholz, V. Holý, and T. Jungwirth, Nat. Commun. **7**, 11623 (2016).
[13] S. DuttaGupta, R. Itoh, S. Fukami, and H. Ohno, Appl. Phys. Lett. **113**, 202404 (2018).
[14] S. Fukami, C. Zhang, S. DuttaGupta, A. Kurenkov, and H. Ohno, Nat. Mater. **15**, 535 (2016).
[15] L. Šmejkal, Y. Mokrousov, B. Yan, and A. H. MacDonald, Nat. Phys. **14**, 242 (2018).
[16] H. Chen, Q. Niu, and A. H. MacDonald, Phys. Rev. Lett. **112**, 017205 (2014).
[17] W. Zhang, W. Han, S. H. Yang, Y. Sun, Y. Zhang, B. Yan, and S. S. P. Parkin, Sci. Adv. **2**, e1600759 (2016).
[18] Y. Zhang, Y. Sun, H. Yang, J. Železný, S. S. P. Parkin, C. Felser, and B. Yan, Phys. Rev. B **95**, 075128 (2017).
[19] J. Kübler and C. Felser, Europhys. Lett. **108**, 67001 (2014).
[20] S. Nakatsuji, N. Kiyohara, and T. Higo, Nature (London) **527**, 212 (2015).
[21] A. K. Nayak, J. E. Fischer, Y. Sun, B. Yan, J. Karel, A. C. Komarek, C. Shekhar, N. Kumar, W. Schnelle, J. Kübler, C. Felser, and S. S. P. Parkin, Sci. Adv. **2**, e1501870 (2016).
[22] T. Higo, H. Man, D. B. Gopman, L. Wu, T. Koretsune, O. M. J. van 't Erve, Y. P. Kabanov, D. Rees, Y. Li, M. T. Suzuki, S. Patankar, M. Ikhlas, C. L. Chien, R. Arita, R. D. Shull, J. Orenstein, and S. Nakatsuji, Nat. Photonics **12**, 73 (2018).
[23] A. Markou, J. M. Taylor, A. Kalache, P. Werner, S. S. P. Parkin, and C. Felser, Phys. Rev. Mater. **2**, 051001(R) (2018).
[24] K.-i. Imakita, M. Tsunoda, and M. Takahashi, J. Appl. Phys. **97**, 10K106 (2005).
[25] K. O'Grady, L. E. Fernandez-Outon, and G. Vallejo-Fernandez, J. Magn. Magn. Mater. **322**, 883 (2010).
[26] H. N. Fuke, K. Saito, Y. Kamiguchi, H. Iwasaki, and M. Sahashi, J. Appl. Phys. **81**, 4004 (1997).
[27] J. B. S. Mendes, R. O. Cunha, O. Alves Santos, P. R. T. Ribeiro, F. L. A. Machado, R. L. Rodríguez-Suárez, A. Azevedo, and S. M. Rezende, Phys. Rev. B **89**, 140406(R) (2014).
[28] V. Tshitoyan, C. Ciccarelli, A. P. Mihai, M. Ali, A. C. Irvine, T. A. Moore, T. Jungwirth, and A. J. Ferguson, Phys. Rev. B **92**, 214406 (2015).
[29] L. Frangou, S. Oyarzún, S. Auffret, L. Vila, S. Gambarelli, and V. Baltz, Phys. Rev. Lett. **116**, 077203 (2016).
[30] H. Reichlová, D. Kriegner, V. Holý, K. Olejník, V. Novák, M. Yamada, K. Miura, S. Ogawa, H. Takahashi, T. Jungwirth, and J. Wunderlich, Phys. Rev. B **92**, 165424 (2015).
[31] Y. C. Lau, D. Betto, K. Rode, J. M. Coey, and P. Stamenov, Nat. Nanotechnol. **11**, 758 (2016).
[32] Y. W. Oh, S. H. Chris Baek, Y. M. Kim, H. Y. Lee, K. D. Lee, C. G. Yang, E. S. Park, K. S. Lee, K. W. Kim, G. Go, J. R. Jeong, B. C. Min, H. W. Lee, K. J. Lee, and B. G. Park, Nat. Nanotechnol. **11**, 878 (2016).
[33] A. Sakuma, K. Fukamichi, K. Sasao, and R. Y. Umetsu, Phys. Rev. B **67**, 024420 (2003).
[34] H. Reichlová, V. Novák, Y. Kurosaki, M. Yamada, H. Yamamoto, A. Nishide, J. Hayakawa, H. Takahashi, M. Maryško, J. Wunderlich, X. Marti, and T. Jungwirth, Mater. Res. Express **3**, 076406 (2016).
[35] T. Kume, T. Kato, S. Iwata, and S. Tsunashima, J. Magn. Magn. Mater. **286**, 243 (2005).
[36] A. Kohn, A. Kovács, R. Fan, G. J. McIntyre, R. C. C. Ward, and J. P. Goff, Sci. Rep. **3**, 2412 (2013).

[37] S. G. Wang, A. Kohn, C. Wang, A. K. Petford-Long, S. Lee, R. Fan, J. P. Goff, L. J. Singh, Z. H. Barber, and R. C. C. Ward, J. Phys. D: Appl. Phys. **42**, 225001 (2009).
[38] A. A. Jara, I. Barsukov, B. Youngblood, Y.-J. Chen, J. Read, H. Chen, P. Braganca, and I. N. Krivorotov, IEEE Magn. Lett. **7**, 3104805 (2016).
[39] T. Sato, M. Tsunoda, and M. Takahashi, J. Appl. Phys. **95**, 7513 (2004).
[40] C. Tusche, H. L. Meyerheim, N. Jedrecy, G. Renaud, A. Ernst, J. Henk, P. Bruno, and J. Kirschner, Phys. Rev. Lett. **95**, 176101 (2005).
[41] G. R. Harp and S. S. P. Parkin, Thin Solid Films **288**, 315 (1996).
[42] H. B. Nie, S. Y. Xu, S. J. Wang, L. P. You, Z. Yang, C. K. Ong, J. Li, and T. Y. F. Liew, Appl. Phys. A **73**, 229 (2001).
[43] J. Nogués and I. K. Schuller, J. Magn. Magn. Mater. **192**, 203 (1999).
[44] A. E. Berkowitz and K. Takano, J. Magn. Magn. Mater. **200**, 552 (1999).
[45] C. Binek, Phys. Rev. B **70**, 014421 (2004).
[46] F. Radu, A. Westphalen, K. Theis-Bröhl, and H. Zabel, J. Phys.: Condens. Matter **18**, L29 (2006).
[47] T. P. A. Hase, B. D. Fulthorpe, S. B. Wilkins, B. K. Tanner, C. H. Marrows, and B. J. Hickey, Appl. Phys. Lett. **79**, 985 (2001).
[48] H. Ohldag, A. Scholl, F. Nolting, E. Arenholz, S. Maat, A. T. Young, M. Carey, and J. Stöhr, Phys. Rev. Lett. **91**, 017203 (2003).
[49] U. Nowak, K. D. Usadel, J. Keller, P. Miltényi, B. Beschoten, and G. Güntherodt, Phys. Rev. B **66**, 014430 (2002).
[50] J. Keller, P. Miltényi, B. Beschoten, G. Güntherodt, U. Nowak, and K. D. Usadel, Phys. Rev. B **66**, 014431 (2002).
[51] F. Nolting, A. Scholl, J. Stöhr, J. W. Seo, J. Fompeyrine, H. Siegwart, J. P. Locquet, S. Anders, J. Lüning, E. E. Fullerton, M. F. Toney, M. R. Scheinfein, and H. A. Padmore, Nature (London) **405**, 767 (2000).
[52] H. Ohldag, T. J. Regan, J. Stöhr, A. Scholl, F. Nolting, J. Lüning, C. Stamm, S. Anders, and R. L. White, Phys. Rev. Lett. **87**, 247201 (2001).
[53] J. van Driel, F. R. de Boer, K. M. H. Lenssen, and R. Coehoorn, J. Appl. Phys. **88**, 975 (2000).
[54] A. Migliorini, B. Kuerbanjiang, T. Huminiuc, D. Kepaptsoglou, M. Muñoz, J. L. F. Cuñado, J. Camarero, C. Aroca, G. Vallejo-Fernández, V. K. Lazarov, and J. L. Prieto, Nat. Mater. **17**, 28 (2018).
[55] M. Tsunoda, T. Sato, T. Hashimoto, and M. Takahashi, Appl. Phys. Lett. **84**, 5222 (2004).
[56] H. Takahashi, Y. Kota, M. Tsunoda, T. Nakamura, K. Kodama, A. Sakuma, and M. Takahashi, J. Appl. Phys. **110**, 123920 (2011).
[57] M. Ali, C. H. Marrows, M. Al-Jawad, B. J. Hickey, A. Misra, U. Nowak, and K. D. Usadel, Phys. Rev. B **68**, 214420 (2003).
[58] H. Katsumi, N. Ryoichi, H. Hiroyuki, S. Yutaka, and T. Shigeru, Jpn. J. Appl. Phys. **35**, 607 (1996).
[59] M. Tsunoda, K.-i. Imakita, M. Naka, and M. Takahashi, J. Magn. Magn. Mater. **304**, 55 (2006).
[60] K.-i. Imakita, M. Tsunoda, and M. Takahashi, Appl. Phys. Lett. **85**, 3812 (2004).
[61] S. S. P. Parkin and V. S. Speriosu, in *Magnetic Properties of Low Dimensional Systems II*, Springer Proceedings in Physics, edited by L. M. Falicov, F. Mejia-Lira, and J. L. Moran-Lopez (Springer, Berlin, 1990), p. 110.
[62] E. Arenholz and K. Liu, Appl. Phys. Lett. **87**, 132501 (2005).
[63] W. Zhang and K. M. Krishnan, J. Appl. Phys. **111**, 07D712 (2012).
[64] J. McCord, R. Schäfer, R. Mattheis, and K. U. Barholz, J. Appl. Phys. **93**, 5491 (2003).
[65] J. M. Taylor, E. Lesne, A. Markou, F. K. Dejene, P. K. Sivakumar, S. Pöllath, K. G. Rana, N. Kumar, C. Luo, H. Ryll, F. Radu, F. Kronast, P. Werner, C. H. Back, C. Felser, and S. S. P. Parkin, arXiv:1904.04797 [Appl. Phys. Lett. (to be published)].